Electro-Oxidation of Borohydride on Rhodium, Iridium, and Rhodium–Iridium Bimetallic Nanoparticles with Implications to Direct Borohydride Fuel Cells

V. Kiran,[a] T. Ravikumar,[a] N. T. Kalyanasundaram,[a] S. Krishnamurty,[c] A. K. Shukla,[b] and S. Sampath[a,z]

[a]*Department of Inorganic and Physical Chemistry and* [b]*Solid State and Structural Chemistry Unit, Indian Institute of Science, Bangalore-560 012, India*
[c]*Central Electrochemical Research Institute, Karaikudi-630 006, India*

Electrochemical oxidation of borohydride is studied on nanosized rhodium, iridium, and bimetallic rhodium–iridium catalysts supported onto Vulcan XC72R carbon. The catalysts are characterized by X-ray diffraction, transmission electron microscopy, and X-ray photoelectron spectroscopy in conjunction with cyclic voltammetry and polarization studies. The studies reveal that a 20 wt % bimetallic Rh–Ir catalyst supported on carbon (Rh–Ir/C) is quite effective for the oxidation of borohydride. Direct borohydride fuel cell with Rh–Ir/C as the anode catalyst and Pt/C as the cathode catalyst exhibits a peak power density of 270 mW/cm^2 at a load current density of 290 mA/cm^2 as against 200 mW/cm^2 at 225 mA/cm^2 for Rh/C and 140 mW/cm^2 at 165 mA/cm^2 for Ir/C while operating at 80°C. The synergistic catalytic activity for the bimetallic Rh–Ir nanoparticles toward borohydride oxidation is corroborated by density-functional theory calculations using electron-localization function.
© 2010 The Electrochemical Society.   [DOI: 10.1149/1.3442372] All rights reserved.

In recent years, considerable interest is evinced in using sodium tetrahydridoborate or sodium borohydride ($NaBH_4$) with a hydrogen content of approximately 11 wt % for directly fueling polymer electrolyte fuel cells (PEFCs). Such PEFCs are referred to as direct borohydride fuel cells (DBFCs).[1-12] In a DBFC, an alkaline solution of $NaBH_4$ is fed to the anode, which is oxidized to $[B(OH)_4]^-$, delivering electrical energy. Indig and Snyder[6] were the first to propose a DBFC in 1962, and subsequent research[7-12] has revived considerable interest in DBFCs. The theoretical open-circuit voltage for the DBFC, with oxygen as the oxidant, is 1.64 V and lies between 2.11 and 3.02 V, with hydrogen peroxide as the oxidant depending upon the pH of the catholyte (see Appendix).[1-4] [d] Nevertheless, the experimentally observed values may be due to mixed potentials, and most likely, fuel crossover may jeopardize the observed potential differences.

Nanostructured catalysts have been gaining interest owing to their attractive electrical and chemical properties. Bimetallic nanoparticles are particularly relevant to the field of catalysis because they often exhibit better catalytic activities than the constituent metals.[14-18] The presence of another metal in the parent lattice affects both the electronic nature and the crystal structure, which in turn influence the catalytic behavior of bimetallic nanoparticles. Rhodium (Rh) and iridium (Ir) metals are good electrocatalysts for various electrochemical reactions, including oxygen reduction reaction (ORR).[19,20] It is also reported that the enhanced activity of the platinum catalyst toward ORR is brought about by its alloying with the other metals.[21] Alloying Rh and Ir, which have almost similar lattice constants, may as well yield a highly homogeneous material with possibly different physical properties in relation to the parent elements.

In the present study, ameliorated electrochemical oxidation of borohydride on bimetallic rhodium–iridium nanostructured catalysts has been studied, and density-functional theory (DFT) calculations are performed to corroborate the experimental findings.

[z] E-mail: sampath@ipc.iisc.ernet.in

[d] The theoretical voltage for DBFCs under the conditions employed in this study, namely, anolyte as alkaline $NaBH_4$ at pH ~14 and catholyte as acidic peroxide at pH ~1,[1,13] would be ~2.95 V vs NHE. In a fuel cell employing ionically conducting membranes, such as the one used in the present study, there can be movement of more than one ion in the membrane, and hence the theoretical voltages need to be calculated by accounting for the pH of the electrolytes and the reactions in the membrane-divided compartments. Accordingly, the values are only indicative and are only used for comparing the actual potentials observed experimentally during the study.

Experimental

Materials.— Rhodium chloride ($RhCl_3 \cdot 3H_2O$), poly(vinylpyrrolidone) (PVP), and Nafion (5 wt % solution in lower aliphatic alcohols/H_2O mixture) were obtained from Aldrich. Chloroiridic acid (H_2IrCl_6) and Pt-loaded carbon (40 wt % Pt/C) were products of Arora Matthey, India. Sodium hydroxide and $NaBH_4$ (AnalaR grade) were obtained from Polysales, India and were used as received. Vulcan XC72R carbon was obtained from Cabot Corporation. All solutions were prepared using Millipore water (Nanopure, 18.2 MΩ).

Synthesis of colloidal Rh, Ir, and Rh–Ir catalyst nanoparticles.— Colloidal nanoparticles of Rh, Ir, and bimetallic Rh–Ir stabilized by PVP were prepared by one-step borohydride reduction using solutions of $RhCl_3$, H_2IrCl_6, and ($RhCl_3$ + H_2IrCl_6), respectively. All the catalysts were prepared with 20 wt % metal loading on Vulcan XC72R carbon support. For example, to prepare a Rh-metal colloid, $RhCl_3$ and PVP (Mw = 55,000) were dissolved in 50 mL of water. Subsequently, freshly prepared sodium borohydride (10 mg) solution (5 mL) was added with stirring. A deep-dark-colored solution was obtained after 3 h, indicating the formation of a metal colloid. An Ir-metal colloid was obtained from H_2IrCl_6 in a similar manner, except that the colloid was heated at 80°C for 3 h after the addition of borohydride. A bimetallic Rh–Ir colloid was prepared by using a 2:1 molar ratio of $RhCl_3$ and H_2IrCl_6 salts.

The metal colloids were added dropwise to a stirred suspension of Vulcan XC72R carbon support in 100 mL water with continuous stirring for 12 h. The carbon-supported colloidal suspensions (Rh/C, Ir/C, and Rh–Ir/C) were then washed copiously with ethanol and distilled water to remove unreacted reducing and stabilizing agents, followed by drying under vacuum at 30°C for 12 h. Finally, the samples were heated in air at 300°C for 30 min before use.

Physical characterization of Rh, Ir, and Rh–Ir catalyst nanoparticles.— The as-prepared Rh, Ir, and Rh–Ir nanoparticles supported on Vulcan XC72R carbon were characterized by powder X-ray diffraction (XRD) (Philips, The Netherlands) and transmission electron microscopy (TEM) (FEI, Philips, Technai F30 TEM) techniques. Samples for TEM analysis were prepared by drop-casting the ultrasonic dispersion of the colloids in ethanol onto carbon-coated copper grids. The energy dispersive X-ray analysis (EDAX) was carried out to decipher the composition of the bimetallic colloid. The supported catalysts were probed using X-ray photoelectron spectros-
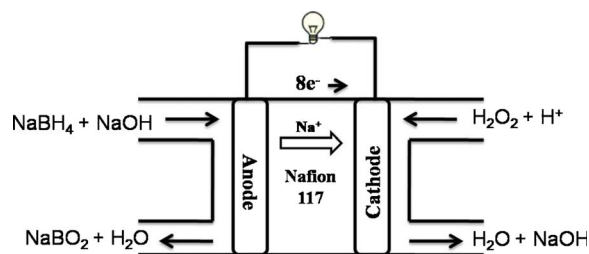
Figure 1. (Color online) Schematic diagram of a DBFC with hydrogen peroxide as the oxidant.

copy (XPS) (Thermofisher Scientific, U.K.) to evaluate the oxidation states of the elements, and Mg Kα radiation (1253.6 eV) was used as the source.

Electrochemical measurements.— Electrochemical studies were performed using an electrochemical workstation (CH660A) with a conventional three-electrode arrangement comprising carbon-supported Rh or Ir or Rh–Ir coated onto a glassy carbon (GC) disk electrode (5 mm diameter) as the working electrode and large Pt foil and Hg/HgO, OH⁻ (1 M KOH) (mercury/mercuric oxide electrode, MMO), as counter and reference electrodes, respectively. The GC electrode was polished with alumina slurry, followed by sonication and washing with distilled water before applying the colloid on its surface. A mixture of 5 mg of Rh/C, Ir/C, or Rh–Ir/C dispersed in 10 μL of 5 wt % Nafion, 1 mL of ethanol was sonicated, and the suspension (10 μL) was carefully applied onto the polished GC electrode surface to obtain constant catalyst loading of 50 μg/cm² of the metal. The dispersed catalyst layer on the GC surface was dried in hot air for 2 h before use. Varying concentrations of $NaBH_4$ were used in 1 M NaOH as the supporting electrolyte. Before all electrochemical experiments, the electrolyte was de-aerated by purging with Ar gas for about 20 min.

Preparation of MEA for fuel cells.— Electrochemical polarization studies on DBFCs were performed using a GSTAT 101P galvanostat (Technoscience, India). Membrane electrode assemblies (MEAs) were obtained by sandwiching a pretreated Nafion-117 membrane between the anode and the cathode, as reported earlier.[22] The schematic diagram of the DBFC is shown in Fig. 1.

Preparation of anode.— A slurry of Rh/C, Ir/C, or Rh–Ir/C catalyst was obtained by ultrasonicating Rh/C, Ir/C, or Rh–Ir/C mixed with 7 wt % Nafion in cyclohexane and was pasted on Toray carbon paper of 0.28 mm thickness. The loading of the catalyst was kept at 0.5 mg/cm².

Preparation of cathode.— The cathode catalyst layer was prepared by dispersing required amount of 40 wt % Pt/C in 7 wt % Nafion solution in cyclohexane, and the slurry thus obtained was coated onto Toray carbon paper followed by drying in air. The loading of the cathode catalyst was kept at 2 mg/cm². The MEAs were obtained by hot-pressing the cathode and anode on either side of a pretreated Nafion-117 membrane at a pressure of 0.4 ton at 125°C for 3 min.

In the DBFCs, the anode and cathode of the MEAs were in contact with high density graphite blocks into which gas/liquid flow-field channels were machined to achieve minimum mass polarization. The ridges between the channels made electrical contact to the carbon electrode with a geometric area of 4.84 cm². The channels supplied alkaline sodium borohydride (1.35 mL min⁻¹) to the anode and acidic (sulfuric acid) hydrogen peroxide (2.1 mL min⁻¹) to the cathode using peristaltic pumps. Electrical heaters were mounted at the end of stainless steel plates behind each of the graphite blocks to maintain the desired cell temperature.

The utilization-efficiency values for the fuel and oxidant were obtained while operating the fuel cell with both the fuel and the oxidant in the recirculation mode. The concentrations of the anolyte and catholyte were 2.64 M in 2.5 M NaOH and 2.2 M H_2O_2 in 1.5 M H_2SO_4, respectively. The cell voltage was monitored as a function of time at a constant load current density of 50 mA/cm² until an abrupt change in cell polarization was observed.[23] The utilization efficiency was then obtained by dividing the experimentally observed capacity with its theoretically estimated value.

Computational study.— To understand the improved catalytic activity of borohydride fuel cells with rhodium–iridium binary nanoclusters, the electronic structures of small Rh, Ir, and Rh–Ir mixed clusters were analyzed by DFT. The reported DFT calculations on Rh and Ir clusters were only handful unlike other catalytically active nanoclusters, such as Au and Pt. The calculations revealed that Rh clusters adsorbed on MgO(001) surfaces possessed different electronic properties compared to their bulk counterpart.[24] In the present study, DFT calculations were carried out on model systems of pure and binary clusters. Nanoclusters of Ir, Rh, and Ir–Rh used in the experiments were in the range of 3–5 nm (30–50 Å). However, under identical experimental conditions, Rh/Ir alloy clusters behave differently in relation to pure Rh and Ir clusters, and the difference might come due to alloying, as observed from DFT calculations on several metal clusters, namely, Ag–Au [25] and alloys of Pt metal.[26] During alloying, considerable charge redistribution occurs among the atoms in the nanocluster. This charge redistribution or, in other words, the modified electronic structure is the primary reason for the oxidation and reduction properties of nanoclusters.[27] In this study, therefore, attempt was made to follow the charge redistribution through small clusters as a model (cluster size ~1 nm). Although semiempirical methods could be used for modeling large periodic systems, these methods are not accurate enough for an understanding of the charge redistribution due to the absence of differential overlap. This is especially so for the transition metals where the explicit description of d electrons is important. Furthermore, periodic models are not balanced representations of the finite-sized nanoclusters, whose properties arise from the quantum confinement of the electrons.[28] Therefore, DFT calculations were conducted to understand the role of alloying when finite-sized clusters are considered. While the size itself might be smaller than those used in experimental conditions, the idea was to understand the underlying electronic implications due to alloying. The DFT studies were carried out using electron-localization function (ELF) to visualize the electron redistribution.[29]

ELF is a measure of the likelihood of finding an electron in the neighborhood.[30,31] ELF $\eta(r)$ is expressed as

$$\eta(r) = \frac{1}{1 + (D/D_h)^2}$$

where

$$D = \frac{1}{2}\sum_{i=1}^{N}|\nabla\psi_i|^2 - \frac{1}{8}\frac{|\nabla\rho|^2}{\rho}$$

$$D_h = \frac{3}{10}(3\pi^2)^{2/3}\rho^{5/3}, \quad \rho = \sum_{i=1}^{N}|\psi_i|^2$$

and all other terms have their usual meanings; $\eta(r)$ is a dimensionless localization index ranging from 0 to 1; the closer its value to 1, the greater the localization of the electron density.

DFT calculations were carried out using VASP (Vienna ab initio simulation package) software in which only the valence electrons were considered.[32,33] The core-valence electron interactions were treated by plane augmented wave pseudopotentials.[34,35] In addition, a generalized gradient approximation of Perdew–Wang was used for all the systems.[30] The plane wave basis set was employed with an energy cutoff of 900 eV, with a convergence in the total energy on the order of ~0.0001 eV. The cluster was placed in a cell with a 10
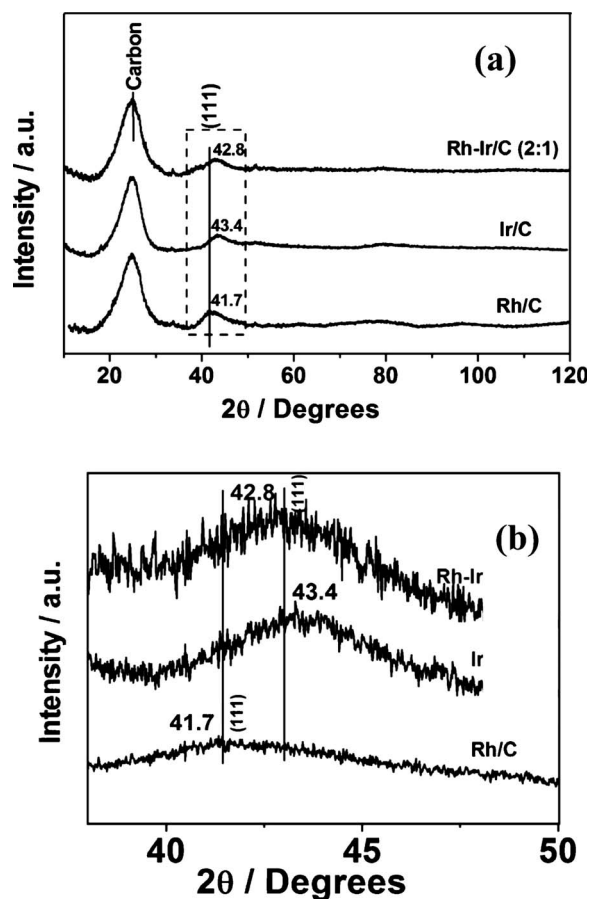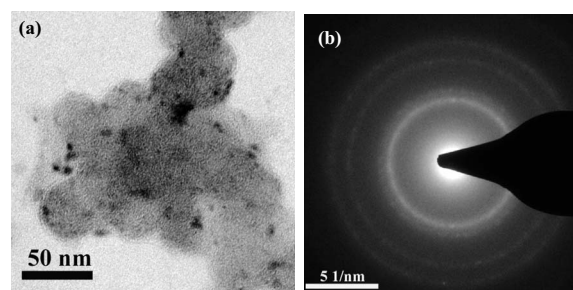
Figure 3. Transmission electron micrograph of Rh–Ir (20 wt %) catalyst: (a) bright-field image and (b) selected area electron diffraction pattern.

al.[37] reported similar peak shifts for the formation of alloy phases. The particle sizes of Rh, Ir, and Rh–Ir obtained using the Debye–Scherrer equation are given in Table I.

TEM.— It is observed in Fig. 3 that Rh–Ir catalyst nanoparticles have an average diameter of 4.3 ± 0.4 nm, as determined by the particle size distribution, shown in Fig. 4, by counting about 150 particles. The appearance of rings observed in the selected area electron diffraction pattern for Rh–Ir/C indicates the particles to be crystalline. Carbon-supported Rh–Ir nanoparticles are further probed by energy-filtered TEM to obtain information on the chemical nature of the sample. The rhodium and iridium elemental mapping data (not included) clearly indicate that each particle contains both rhodium and iridium phases and supports the formation of an alloy. EDAX analysis of Rh–Ir reveals 70 atom % of Rh and 30 atom % of Ir, confirming the 2:1 ratio of Rh and Ir based on the composition of the starting solution. The average sizes are given in Table I.

XPS.— Figure 5 shows the spectra of Rh (3d) and Ir (4f) levels obtained for individual as well as alloy nanoparticles supported onto carbon. The deconvoluted spectra show four peaks for both pristine Rh and Rh–Ir alloy nanoparticles, as depicted Fig. 5a and b. As shown in Fig. 5a, the observed binding energy (BE) values of 307.4 and 312.2 eV correspond to Rh $3d_{5/2}$ and Rh $3d_{3/2}$ levels of rhodium nanoparticles in metallic state (Rh^0). The values agree with the values reported,[38] while the BE obtained for rhodium levels in the alloy nanoparticles are very similar, namely, 307.5 and 311.9 eV. The other Rh BE values observed at 309.3 and 314 eV for pure samples and at 309.4 and 313.5 eV for Rh–Ir samples are consistent with the oxidized species of rhodium, namely, Rh_2O_3.[39,40] The relative ratios of concentrations reveal that Rh is present predominantly
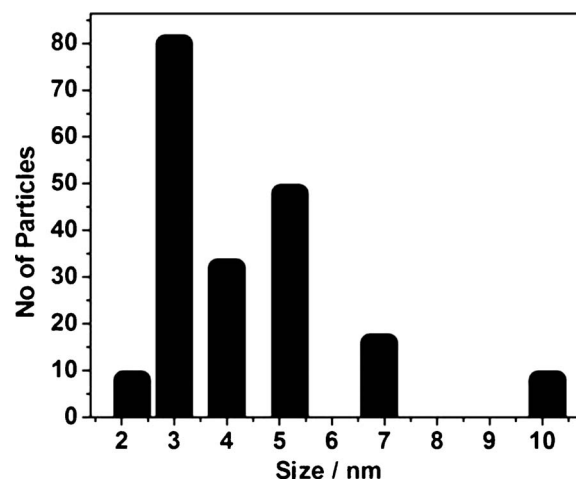

Figure 4. Particle size distribution for carbon-supported Rh–Ir (20 wt %) catalyst.

Figure 2. (a) Powder XRD patterns for 20 wt % carbon-supported Rh, Ir, and Rh–Ir and (b) amplified part of [111] reflection.

Å distance between the neighboring images. The convergence for the energy cutoff and the cell size was found by gradual increments in energy cutoff values and cell size.

Results and Discussion

XRD.— Catalysts supported on carbon are stable over prolonged periods without any degradation. The powder XRD patterns for carbon-supported Rh, Ir, and Rh–Ir (2:1) are shown in Fig. 2a and b. The data depict broad peaks that match well with the diffraction patterns for face-centered cubic (fcc) phases for Rh and Ir. The peak broadening suggests that the crystallites are very small and finely dispersed. The peak at $2\theta = 24.8°$, which is characteristic of graphitic carbon, is observed for all the catalysts. The peak corresponding to the (111) plane for pristine Rh is observed at $2\theta = 41.7°$, and that for pristine Ir is observed at $2\theta = 43.4°$. The peak corresponding to the Rh(111) plane for the bimetallic Rh–Ir/C catalyst is observed at $2\theta = 42.8°$, as shown in Fig. 2b. The shift in (111) diffraction peak in Rh–Ir/C in relation to pristine Rh/C confirms the formation of Rh-Ir alloy in Rh-Ir/C. Geng and Lu[36] and Selvarani et

Table I. Average particle sizes for various catalysts obtained from XRD and TEM.

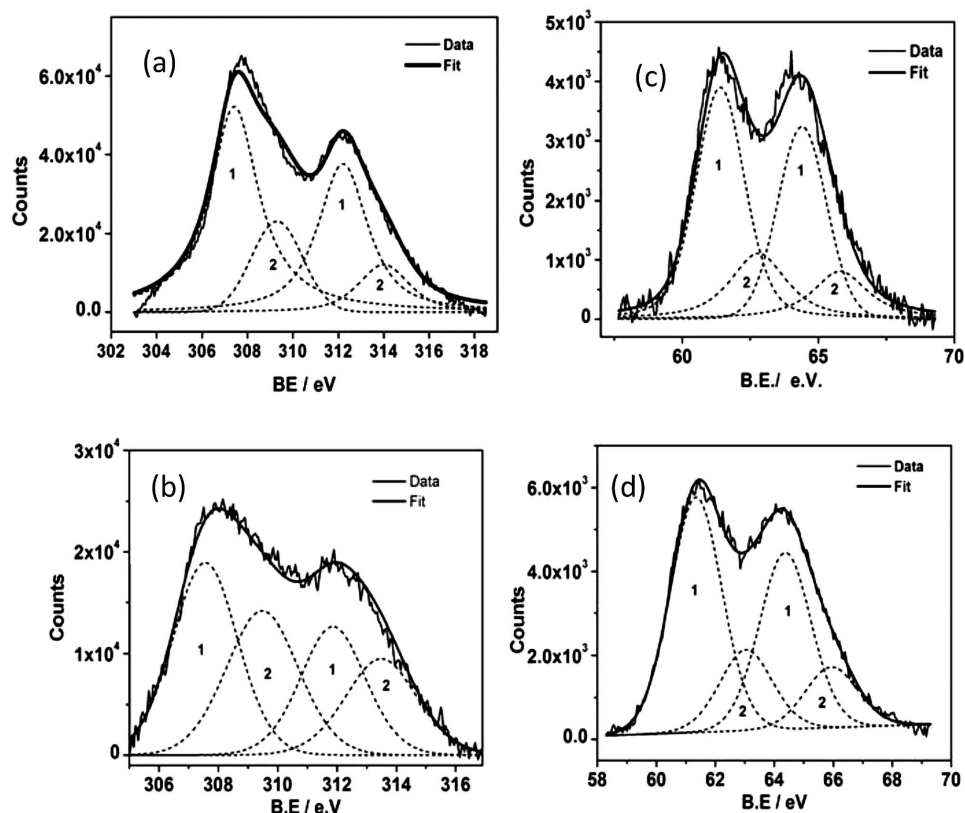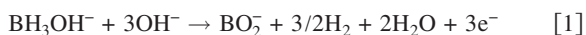| Catalyst	Average particle size by XRD (nm)	Average particle size by TEM (nm)
Rh/C	4.3	3.6 ± 1.05
Ir/C	2.3	1.95 ± 0.8
Rh–Ir/C	5.4	4.3 ± 0.4

Figure 5. Rh 3d XPS spectra for carbon-supported (a) Rh and (b) Rh–Ir catalysts; Ir (4f) XPS spectra of carbon-supported (c) Ir and (d) Rh–Ir nanoparticles. 1 and 2 correspond to metallic and oxidized species, respectively.

in the metallic state in pure Rh, while the alloy nanostructures have both metallic and oxidized states of Rh almost in equal concentrations. The Ir (4f) deconvoluted spectra for pristine Ir and alloy (Rh–Ir) nanostructures are shown in Fig. 5c and d. The spectra indicate the presence of Ir^0 species with BE values at 61.3 and 64.3 eV for pristine Ir and at 61.4 and 64.4 eV for Ir in Rh–Ir, corresponding to Ir $4f_{7/2}$ and Ir $4f_{5/2}$ levels, respectively. The relative ratios reveal that Ir^0 species is predominant compared to Ir^{4+} and is based on the reported BE values.[41]

Cyclic voltammetry studies.— Cyclic voltammograms are recorded on Rh, Ir, and Rh–Ir catalyst nanoparticles coated on GC electrodes. Figure 6 shows the effect of varying concentrations of $NaBH_4$ in deoxygenated 1 M aqueous NaOH in the potential range between −0.8 and 0.4 V. Two oxidation peaks, as depicted in Fig. 6b, are observed for Rh/C catalysts in the potential range between −0.7 and 0.1 V in the forward direction. Martins et al.[42] made similar observations on Pt electrode in alkaline solutions, and the peaks are assigned to the oxidation of BH_3OH^- at −0.42 V vs Ag/AgCl produced by chemical hydrolysis of BH_4^- and to the direct oxidation of BH_4^- at −0.13 V. In the present study, the peak observed in the range between −0.7 and −0.2 V (vs MMO) may be due to the oxidation of BH_3OH^-, as shown below

$$BH_3OH^- + 3OH^- \rightarrow BO_2^- + 3/2H_2 + 2H_2O + 3e^- \qquad [1]$$

The latter peak between −0.2 and 0.1 V appears to be due to the direct oxidation of BH_4^-. During the reverse scan, an oxidation peak is observed at −0.65 V and is likely to be due to the oxidation of BH_3OH^- formed during the direct oxidation of BH_4^- in the forward scan, as reported for Au and Pt.[43-45]

Figure 6c depicts the cyclic voltammograms for Ir/C electrode. Only one oxidation peak at −0.32 V is observed in the potential range studied. The peak increases with an increase in the concentration of $NaBH_4$ from 0.01 to 0.1 M. Accordingly, the peak at −0.32 V appears to be due to the direct oxidation of BH_4^-. During the

reverse scan, an oxidation peak is observed at −0.43 V due to the oxidation of BH_3OH^- formed during the oxidation of BH_4^- in the forward reaction.

The voltammograms observed on colloidal Rh–Ir/C catalyst are shown in Fig. 6a. On alloying Rh with Ir, the electrocatalytic activity toward borohydride oxidation increases with the behavior similar to that observed with monometallic Rh. Two peaks are observed: one between −0.5 and −0.2 V due to the oxidation of chemically formed BH_3OH^- and the other between −0.1 and 0.1 V due to the
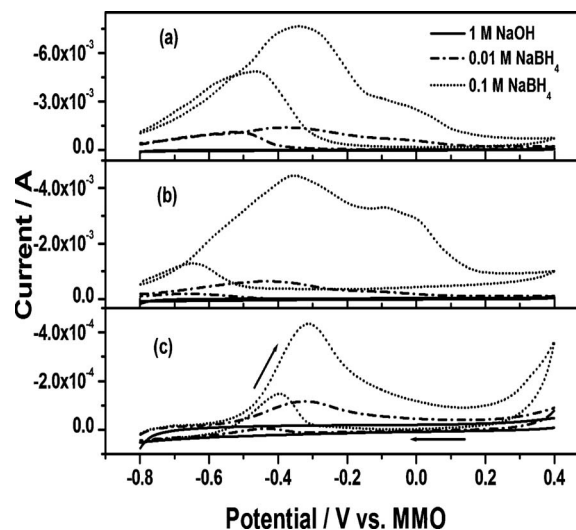

Figure 6. Cyclic voltammograms of BH_4^- oxidation on colloidal (a) Rh–Ir, (b) Rh, and (c) Ir catalysts immobilized on GC electrode at 25°C. Supporting electrolyte: 1 M NaOH. Scan rate = 0.05 V s^{-1}.
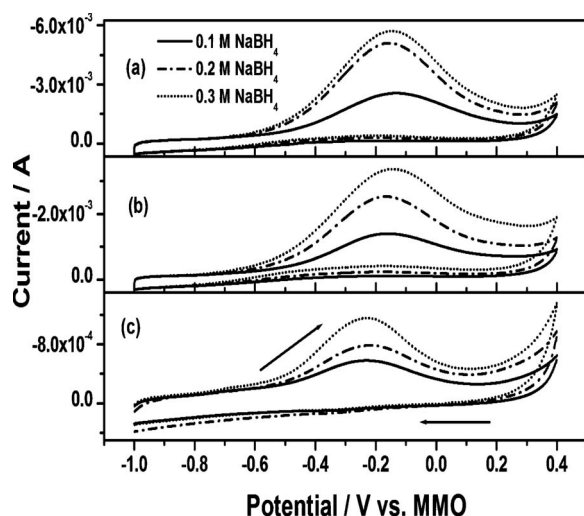
Figure 7. Cyclic voltammograms showing the effect of BH_4^- concentration on colloidal (a) Rh–Ir, (b) Rh, and (c) Ir immobilized on GC. Supporting electrolyte: 1 M NaOH in presence of 1.5×10^{-3} M thiourea. Scan rate = 0.05 V s^{-1}.

direct oxidation of BH_4^-. During the cathodic scan, an additional oxidation peak is observed at a peak potential of -0.5 V for the oxidation of BH_3OH^- akin to Rh and Ir.

The suppression of hydrogen evolution is an important consideration and is generally affected by the use of thiourea.[45] Experiments have been carried out in the presence of 1.5×10^{-3} M thiourea, and the voltammograms are shown in Fig. 7a-c. The voltammograms indicate only one peak at -0.15 V for Rh and Rh–Ir while the value is close to -0.2 V for Ir and are attributed to the direct oxidation of BH_4^-. The suppression of hydrogen evolution/chemical formation of BH_3OH^- is observed in the present studies as well.

From the foregoing discussion based on Fig. 7, it can be surmised that among the investigated colloidal catalysts, Rh–Ir/C exhibits the highest oxidation currents. By contrast, Ir/C exhibits the least activity. The concentration dependence of direct borohydride oxidation peak current in the presence of thiourea at (-0.15 V vs MMO) is linear for all the three catalysts. The oxidation currents for the first scan increase linearly with the square root of the scan rate, indicating a diffusion-controlled process.

Fuel cell performance.— Utility of the nanosized catalysts in fuel cells is probed using $NaBH_4$ as the anolyte and hydrogen peroxide as the catholyte. To find the optimum concentration of $NaBH_4$, varying concentrations of $NaBH_4$ between 1.32 and 3.97 M are fed to the anode at a flow rate of 1.35 mL/min, keeping all other parameters such as temperature, catalyst loading, and concentration of H_2O_2 at the cathode constant. The results are shown in Table II. A peak power density of 102 mW/cm² at 25°C with 2.64 M $NaBH_4$ is obtained for the Rh–Ir-based cell.

Above 2.64 M $NaBH_4$ concentration, both peak power density and sustained current density decrease, and it is likely that at high concentrations, the crossover of $NaBH_4$ from anode to cathode side may become appreciable.[46] The crossed-over $NaBH_4$ could be oxidized on Pt catalyst at the cathode side, lowering the cell potential. The mixed potential at the cathode has been reported to decrease the overall performance of the DBFC.[7,9,46] The optimum concentration of borohydride is 2.64 M $NaBH_4$.

The polarization data for DBFC-I (Rh/C), DBFC-II (Ir/C), and DBFC-III (Rh–Ir/C) cells obtained for varying temperatures with the optimized $NaBH_4$ concentration are shown in Fig. 8a-c. It is evident that the peak power-density and sustained current-density values for the DBFCs increase with increasing temperature, as reported for other borohydride-based fuel cells.[9,10]

Anode and cathode polarization studies were performed to determine individual electrode performances. The studies were carried out by placing the MMO reference electrode in the anode chamber, and the anode potential was monitored against MMO as a function of current density; the data are shown in Fig. 9. Cathode potentials were obtained by subtracting anode potentials from the cell voltage. It is evident in Fig. 9 that the cathode suffers higher polarization losses than the anode. The potential of the cathode at zero current is around 0.9 V vs normal hydrogen electrode (NHE), suggesting a mixed potential as peroxide is reduced by a two-step process, namely, the reduction of oxygen produced by the decomposition of peroxide as well as the direct reduction of peroxide. The theoretical cell potentials associated with the two processes are 0.4 and 1.77 V vs NHE, respectively.[4] The cathode potentials show large polarization losses that render the DBFCs limited by the cathode kinetics, i.e., peroxide reduction.[1,4,10] Similar behaviors have been observed for DBFCs based on Rh/C and Ir/C, but the data are not included for the sake of brevity.

Efficiency.— The utilization-efficiency values for the fuel cells are determined as given below. The theoretical capacity of $NaBH_4$ fuel is 11.4 Ah/mol for an eight-electron-transfer reaction. The experimentally observed capacity is about 1.22 Ah for the Rh–Ir/C cell, which is 10.7% of the theoretical value. Similarly, the efficiencies for Rh/C- and Ir/C-based cells are 8.1 and 7.1%, respectively, as depicted in Fig. 10. The low efficiency values may be due to the loss of borohydride as H_2 by hydrolysis. Other reasons for the reduced efficiency may include crossover as well as the presence of unreacted borohydride. Similar observations were reported by Jamard et al.[47] However, it is quite evident that the cell voltage for all DBFCs is quite stable for about 4–5 h even while using the fuel and the oxidant in recirculation mode.

Computational details and model clusters.— To obtain first-level information on the reasons for the better performance of Rh–Ir than the individual Rh and Ir catalysts, DFT calculations were carried out using six-atom rhodium and iridium clusters. The binary cluster was modeled using Rh_4Ir_2 to reflect the ratio used in the experiments (Rh:Ir ~ 2:1). The lowest geometry is a simple cubic structure for both homogeneous (Rh_6, Ir_6) and mixed clusters (Rh_4Ir_2). Calculations were also carried out with a 20-atom tetrahedral cluster ($Rh_{14}Ir_6$), with its four faces resembling an fcc (111) structure.

The electron distribution around these clusters is analyzed using ELF, which is a well established practical tool to understand the

Table II. Performance data for DBFC-I (Rh/C), DBFC-II (Ir/C), and DBFC-III (Rh–Ir/C) cells at 25°C with varying concentrations of $NaBH_4$ (in 2.5 M NaOH) at the anode and 2.2 M H_2O_2 (in 1.5 M H_2SO_4) at the cathode. Anode loading: 0.5 mg/cm². Cathode loading: 2 mg/cm².

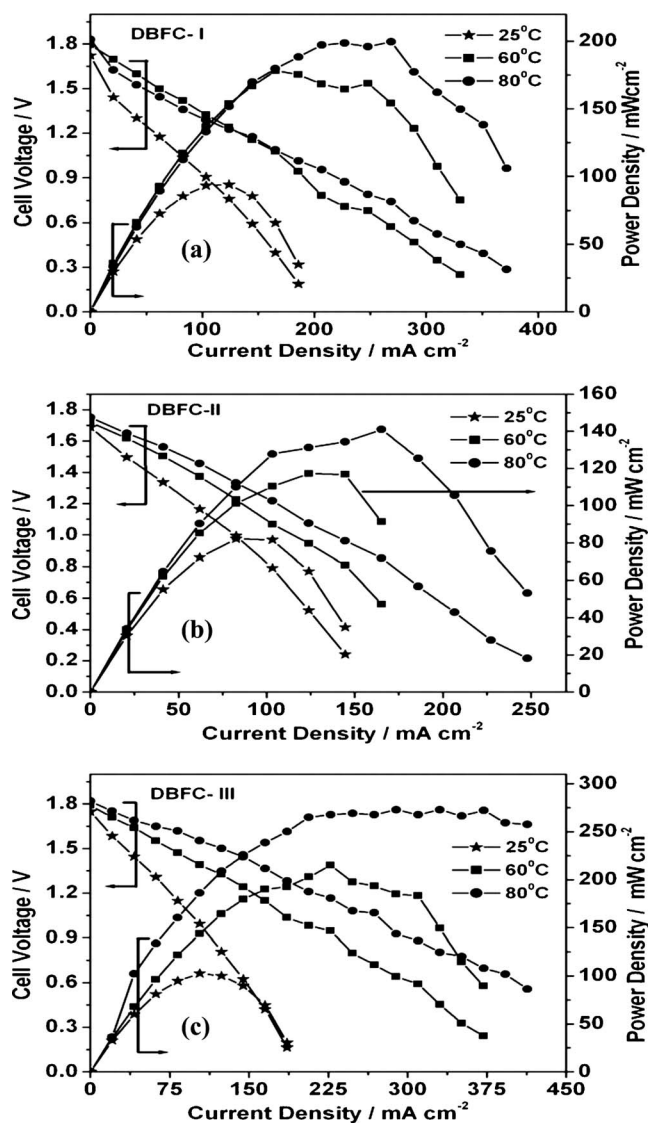| Concentration of BH_4^-	DBFC-I (Rh/C)		DBFC-II (Ir/C)		DBFC-III (Rh–Ir/C)	
	Power density (mW cm⁻²)	Current density (mA cm⁻²)	Power density (mW cm⁻²)	Current density (mA cm⁻²)	Power density (mW cm⁻²)	Current density (mA cm⁻²)
1.32 M	68	82	54	62	76	93
2.64 M	92	93	80	82	102	103
3.97 M	79	82	76	72	85	93

Figure 8. Polarization data for (a) DBFC-I (Rh/C), (b) DBFC-II (Ir/C), and (c) DBFC-III (Rh–Ir/C) cells at varying temperatures. Anolyte is 2.64 M NaBH$_4$ in 2.5 M NaOH, and catholyte is 2.2 M H$_2$O$_2$ in 1.5 M H$_2$SO$_4$. Anode loading: 0.5 mg/cm^2. Cathode loading: 2 mg/cm^2.

Figure 9. Individual anode and cathode polarization data for DBFC-III (Rh–Ir/C) cell at 25°C and 60°C. Anolyte is 2.64 M NaBH$_4$ in 2.5 M NaOH, and catholyte is 2.2 M H$_2$O$_2$ in 1.5 M H$_2$SO$_4$. Anode loading: 0.5 mg/cm^2. Cathode loading: 2 mg/cm^2.

precise type of bonding between atoms within a cluster or molecule. Table III shows the geometric and electronic properties of six-atom clusters. The Rh–Rh bond distances in both homogeneous and mixed clusters (∼2.5 Å) are smaller than their bulk counterparts (∼2.8 Å). The electronic configuration of Rh is 4d^8 and 5s^1. In clusters, the 4d and 5s orbitals hybridize, which leads to short bond distances. This is clearly observed from the charge-density contours of Rh$_6$ given in Fig. 11a. This is true in iridium clusters as well (figure not shown) where the 5d^7 and 6s^2 orbitals hybridize, resulting in short bond distances compared to its bulk counterpart. This hybridization leads to localized electron distribution in homogeneous clusters with some electrons localized at an isovalue of 0.70, as shown in Fig. 11b. The data also reveal a certain amount of charge density between the bonds, indicating the presence of covalency. However, in the binary clusters of Rh$_4$Ir$_2$, the localization is substantially reduced with just a lone pair of electrons around iridium atoms, as observed in Fig. 11c. This multicenter bonding, which is also referred to as delocalized electron density, results from the pair of electrons involved in bonding three or more atoms. While such an interaction between covalent bonding and a free electron gas
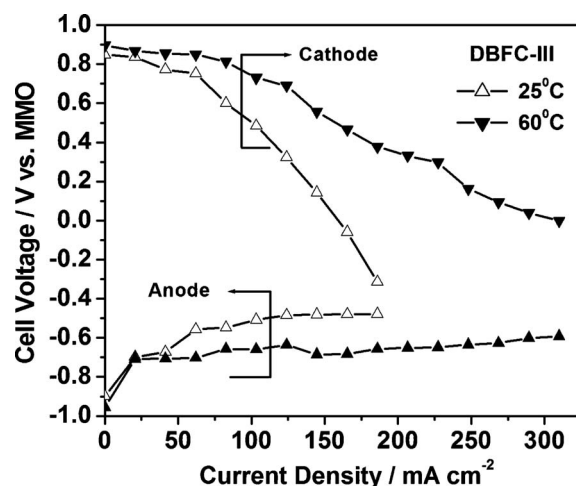
picture depicting a perfectly delocalized electron density distribution has been well established in resonance structures, recent theoretical investigations have revealed its existence in several nanoclusters such as Li.[48] This multicentered bonding has been reported to be a primary reason for high electrical conductivity observed with SnO$_2$.[49] Thus, the pair of delocalized electrons around Ir is easily available for electrical conduction in the binary Rh–Ir clusters. To
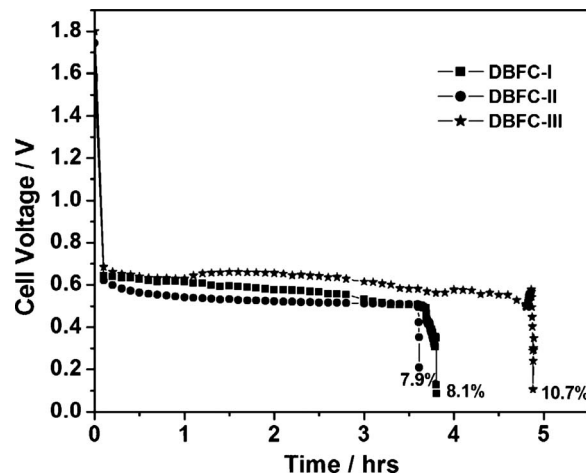

Figure 10. Cell voltage vs time for DBFC-I (Rh/C), DBFC-II (Ir/C), and DBFC-III (Rh–Ir/C) cells at 25°C. Anolyte: 2.64 M NaBH$_4$ in 2.5 M NaOH. Catholyte: 2.2 M H$_2$O$_2$ in 1.5 M H$_2$SO$_4$. Anode loading: 0.5 mg/cm^2. Cathode loading: 2 mg/cm^2. Load current density: 50 mA/cm^2.

Table III. Geometric and electronic properties of six-atom rhodium and iridium clusters obtained from DFT calculations.

Cluster	HOMO–LUMO energy gap (eV)	Rh–Rh bond distance (Å)	Ir–Ir bond distance (Å)	Rh–Ir bond distance (Å)
Rh$_6$	0.271	2.51	—	—
Ir$_6$	0.252	—	2.44	—
Rh$_4$Ir$_2$	0.092	2.54	2.48	2.60
Rh$_{20}$	0.070	2.46	—	—
Ir$_{20}$	0.053	—	2.48	—
Rh$_{14}$Ir$_6$	0.021	2.50	2.52	2.67

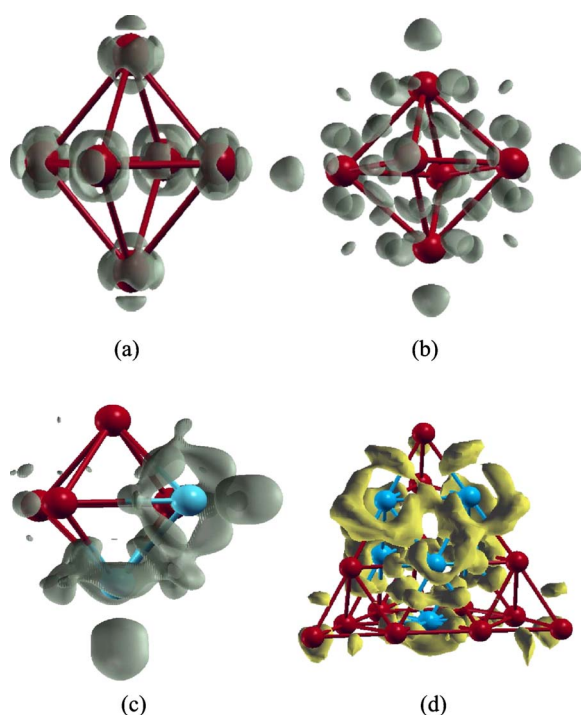**Figure 11.** (Color online) (a) Charge-density distribution for Rh_6 cluster at an isovalue of 2.5 eV/Å^3, (b) ELF for Rh_6 cluster at an isovalue of 0.70, (c) ELF function for Rh_4Ir_2 cluster at an isovalue of 0.70, and (d) ELF function for $Rh_{14}Ir_6$ at an isovalue of 0.70. Rh atoms are shown in red, while the Ir atoms are shown in blue.

validate the results obtained for the Rh_4Ir_2 cluster, we have also analyzed the ELF for a large cluster, viz., $Rh_{14}Ir_6$, which shows a similar multicentered bonding, as shown in Fig. 11d. Ir atoms have higher electron affinity (-151.0 kJ/mol) and higher electronegativity (1.55) than Rh (-110 kJ/mol and 1.45, respectively). Accordingly, Ir atoms in the binary clusters may be expected to absorb some electrons from Rh atoms present in the binary clusters, leading to a high electron distribution around Ir. The higher reactive/conducting nature of the binary clusters than their homogeneous counterparts is also reflected from the energy gap values, as given in Table III. The highest occupied molecular orbital–lowest unoccupied molecular orbital (HOMO–LUMO) energy gap has always been associated with the reactivity of the systems, and a compound with a lower HOMO–LUMO gap is less stable and more reactive.[50]

It is widely accepted that the electronic structure of a cluster is closely related to its catalytic activity.[51] In the present study, we observe multicenter delocalized bonding in alloy clusters akin to that reported earlier in organic compounds and several metal clusters.[52,53] In the latter, the charge density arising from multicenter bonding is quite delocalized and is easily available for transfer.[54] Accordingly, the multicentered bonding observed in Rh–Ir alloy clusters of varying size appears to be responsible for higher catalytic activity in relation to the parent elements. The observed HOMO–LUMO gap, which is a measure of the energy difference between the orbitals responsible for the reactivity/stability of a system[55,56] and is similar to the concept of electron density at the Fermi level in finite-sized systems, is smaller for Rh–Ir in relation to pure Rh or Ir clusters. DFT and the properties derived from its application to nanoclusters, such as charge density and ELF, are established tools for understanding electrocatalytic oxidation/reduction properties of the clusters.[57]

Conclusions

Electrocatalytic activities of carbon-supported Rh, Ir, and Rh–Ir catalysts toward direct oxidation of sodium borohydride in alkaline media have been studied using cyclic voltammetry. Alloying of Rh with Ir improves the electrode kinetics of $NaBH_4$ oxidation in relation to their constituent elements. Fuel cell performance data reflect Rh–Ir/C anode catalysts to exhibit the highest peak power density. Accordingly, carbon-supported Rh–Ir alloy is a potential anode catalyst for DBFCs. DFT calculations corroborate the high catalytic activity of Rh–Ir based on its lower energy gap between HOMO–LUMO than Rh and Ir. model Rh–Ir alloy clusters exhibit multicentered bonding unlike the constituent Rh and Ir clusters.
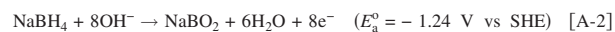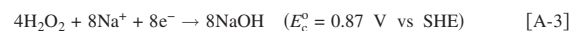
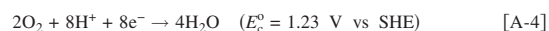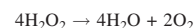## Appendix
Details on Calculations of Cell Potentials for the DBFCs

In the DBFC, alkaline aqueous sodium borohydride is oxidized at the anode to sodium borate according to the following reactions[1,4,6-8]
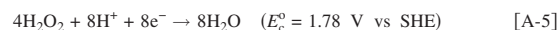
$$8NaOH \leftrightarrow 8Na^+ + 8OH^- \qquad [A-1]$$

$$NaBH_4 + 8OH^- \rightarrow NaBO_2 + 6H_2O + 8e^- \quad (E_a^o = -1.24 \text{ V vs SHE}) \quad [A-2]$$

where SHE denotes standard hydrogen electrode. At the cathode, electroreduction of hydrogen peroxide proceeds as follows

$$4H_2O_2 + 8Na^+ + 8e^- \rightarrow 8NaOH \quad (E_c^o = 0.87 \text{ V vs SHE}) \qquad [A-3]$$

As the pH of the H_2O_2 solution in the catholyte converges to 0, two reactions could take place: (*i*) by decomposition of H_2O_2 to O_2 followed by its reduction as

$$4H_2O_2 \rightarrow 4H_2O + 2O_2$$

$$2O_2 + 8H^+ + 8e^- \rightarrow 4H_2O \quad (E_c^o = 1.23 \text{ V vs SHE}) \qquad [A-4]$$

and (*ii*) by electrochemical reductive decomposition of H_2O_2 as

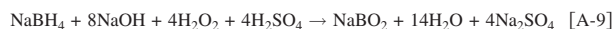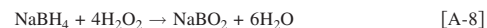$$4H_2O_2 + 8H^+ + 8e^- \rightarrow 8H_2O \quad (E_c^o = 1.78 \text{ V vs SHE}) \qquad [A-5]$$

The respective variation in O_2 and H_2O_2 reduction potentials with pH are governed by

$$E(O_2) = 1.23 - 0.059 \text{ pH} \qquad [A-6]$$

and

$$E(H_2O_2) = 1.78 - 0.059 \text{ pH} \qquad [A-7]$$

Accordingly, the net cell reaction in such a DBFC shifts from

$$NaBH_4 + 4H_2O_2 \rightarrow NaBO_2 + 6H_2O \qquad [A-8]$$

$$NaBH_4 + 8NaOH + 4H_2O_2 + 4H_2SO_4 \rightarrow NaBO_2 + 14H_2O + 4Na_2SO_4 \quad [A-9]$$

Thus, depending on the pH of H_2O_2 solution in the catholyte, the cell potential varies between 2.11 and 3.02 V.[1]

The membrane potential is not included in the aforesaid calculations.

References

1. R. K. Raman, N. A. Choudhury, and A. K. Shukla, *Electrochem. Solid-State Lett.*, **7**, A488 (2004).
2. G. H. Miley, N. Luo, J. Mather, R. Burton, G. Hawkins, L. Gu, E. Byrd, R. Gimlin, P. J. Shrestha, G. Benavides, et al., *J. Power Sources*, **165**, 509 (2007).
3. C. A. Sequeria, T. C. Pardal, D. M. Santos, J. A. Condeco, M. W. Franco, and M. C. Gonacalves, *ECS Trans.*, **3**(18), 37 (2007).
4. C. Ponce de León, F. C. Walsh, A. Rose, J. B. Lakeman, D. J. Browning, and R. W. Reeve, *J. Power Sources*, **164**, 441 (2007).
5. D. Cao, D. Chen, J. Lan, and G. Wang, *J. Power Sources*, **190**, 346 (2009).
6. M. E. Indig and R. N. Snyder, *J. Electrochem. Soc.*, **109**, 1104 (1962).
7. S. C. Amendola, P. Onnerud, M. T. Kelly, P. J. Petillo, S. L. Sharp-Goldman, and M. Binder, *J. Power Sources*, **84**, 130 (1999).
8. Z. P. Li, B. H. Liu, K. Arai, K. Asaba, and S. Suda, *J. Power Sources*, **126**, 28 (2004).
9. H. Cheng and K. Scott, *J. Power Sources*, **160**, 407 (2006).
10. N. A. Choudhury, R. K. Raman, S. Sampath, and A. K. Shukla, *J. Power Sources*, **143**, 1 (2005).
11. C. Ponce de Leon, F. C. Walsh, D. Pletcher, D. J. Browning, and J. B. Lakeman, *J. Power Sources*, **155**, 172 (2006).
12. U. B. Demirci, *J. Power Sources*, **172**, 676 (2007).
13. M. Simões, S. Baranton, and C. Coutanceau, *J. Phys. Chem. C*, **113**, 13369 (2009).

14. A. F. Lee, C. J. Baddeley, C. Hardacre, R. M. Ormerod, R. M. Lambert, G. Schmid, and H. West, *J. Phys. Chem.*, **99**, 6096 (1995).
15. N. Toshima, M. Harada, T. Yonezawa, K. Kushihashi, and K. Asakura, *J. Phys. Chem.*, **95**, 7448 (1991).
16. T. Yonezawa and N. Toshima, *J. Mol. Catal.*, **83**, 167 (1993).
17. M. H. Atwan, C. L. B. Macdonald, D. O. Northwood, and E. L. Gyenge, *J. Power Sources*, **158**, 36 (2006).
18. E. Gyenge, M. Atwan, and D. Northwood, *J. Electrochem. Soc.*, **153**, A150 (2006).
19. D. Cao, A. Wieckowski, J. Inukai, and N. Alonso-Vante, *J. Electrochem. Soc.*, **153**, A869 (2006).
20. G. Liu and H. Zhang, *J. Phys. Chem. C*, **112**, 2058 (2008).
21. J. Zhang, M. B. Vukmirovic, K. Sasaki, A. U. Nilekar, M. Mavrikakis, and R. R. Adzic, *J. Am. Chem. Soc.*, **127**, 12480 (2005).
22. S. Mukerjee and S. Srinivasan, *J. Electroanal. Chem.*, **357**, 201 (1993).
23. R. K. Raman and A. K. Shukla, *Fuel Cells*, **7**, 225 (2007).
24. W. Q. Tian, M. Ge, F. Gu, T. Yamada, and Y. Aoki, *J. Phys. Chem. A*, **110**, 6285 (2006).
25. H. M. Lee, M. Ge, B. R. Sahu, P. Tarakeshwar, and K. S. Kim, *J. Phys. Chem. B*, **107**, 9994 (2003).
26. Y. Shimodaira, T. Taneka, T. Miura, A. Kudo, and H. Kobayashi, *J. Phys. Chem. C*, **111**, 272 (2007).
27. N. K. Jena, K. R. S. Chandrakumar, and S. K. Ghosh, *J. Phys. Chem. C*, **113**, 17885 (2009).
28. *Semiconductor Nanoclusters—Physical, Chemical, Catalytic Aspects*, Studies in Surface Science and Catalysis, Vol. 103, P. V. Kamat and D. Meisel, Editors, Elsevier, Amsterdam (1997).
29. B. Silvi and A. Savin, *Nature (London)*, **371**, 683 (1994).
30. A. D. Becke and K. E. Edgecombe, *J. Chem. Phys.*, **92**, 5397 (1990).
31. A. Savin, *J. Mol. Struct.*, **727**, 127 (2005).
32. G. Kresse and J. Hafner, *J. Phys.: Condens. Matter*, **6**, 8245 (1994).
33. G. Kresse and J. Joubert, *J. Phys. Rev. B*, **59**, 1758 (1999).
34. G. Kresse and J. FurthMuller, *Phys. Rev. B*, **54**, 11169 (1996).
35. P. E. Blöchl, *Phys. Rev. B*, **50**, 17953 (1994).
36. T. D. Geng and G. Lu, *J. Phys. Chem. C*, **111**, 11897 (2007).
37. G. Selvarani, S. V. Selvaganesh, S. Krishnamurthy, G. V. M. Kiruthika, P. Sridhar, S. Pichumani, and A. K. Shukla, *J. Phys. Chem. C*, **113**, 7461 (2009).
38. V. Mévellec, A. Nowicki, A. Roucoux, C. Dujardin, P. Granger, E. Payen, and K. Philippot, *New J. Chem.*, **30**, 1214 (2006).
39. T. L. Barr, *J. Phys. Chem.*, **82**, 1801 (1978).
40. M. Peuckert, *Surf. Sci.*, **141**, 500 (1984).
41. I. S. Park, M. S. Kwon, K. Y. Kang, J. S. Lee, and J. Parka, *Adv. Synth. Catal.*, **349**, 2039 (2007).
42. I. Martins, M. C. Nunes, R. Koch, L. Martins, and M. Bazzaoui, *Electrochim. Acta*, **52**, 6443 (2007).
43. J. A. Gardiner and J. W. Collat, *Inorg. Chem. Soc.*, **4**, 1208 (1965).
44. Y. Okinaka, *J. Electrochem. Soc.*, **120**, 739 (1973).
45. E. Gyenge, *Electrochim. Acta*, **49**, 965 (2004).
46. J. H. Kim, H. S. Kim, Y. M. Kang, M. S. Song, S. Rajendran, S. C. Han, D. H. Jung, and J. Y. Lee, *J. Electrochem. Soc.*, **151**, A1039 (2004).
47. R. Jamard, A. Latour, J. Salomon, P. Capron, and A. M. Beaumont, *J. Power Sources*, **176**, 287 (2008).
48. R. Rousseau and D. Marx, *Phys. Rev. Lett.*, **80**, 2574 (1998).
49. A. K. Singh, A. Janotti, M. Scheffler, and C. G. van de Walle, *Phys. Rev. Lett.*, **101**, 055502 (2008).
50. R. G. Pearson, *Proc. Natl. Acad. Sci. U.S.A.*, **83**, 8440 (1986).
51. W. E. Kaden, T. Wu, W. A. Kunkel, and S. L. Anderson, *Science*, **326**, 826 (2009).
52. M. Orchin, R. S. Macomber, A. R. Pinhas, and R. M. Wilson, *Vocabulary and Concepts of Organic Chemistry*, John Wiley & Sons, New York (2005).
53. D. Y. Zubarev and A. I. Boldyrev, *J. Phys. Chem. A*, **113**, 866 (2009).
54. Y. D. Kim, M. Fishcher, and G. Gentefor, *Chem. Phys. Lett.*, **377**, 170 (2003).
55. Y. Gao, S. Bulusu, and X. C. Zeng, *J. Am. Chem. Soc.*, **127**, 15680 (2005).
56. Y. Gao, A. L. Focsan, Y. Y. Li, and L. D. Kispert, *J. Phys. Chem. A*, **110**, 10091 (2006).
57. R. G. Parr, *Annu. Rev. Phys. Chem.*, **34**, 631 (1983).